J. Cent. South Univ. (2022) 29: 4078−4093
DOI: https://doi.org/10.1007/s11771-022-5205-4

Springer

Damage characteristics of thermally treated granite under uniaxial compression: Insights from active and passive ultrasonic techniques

GUO Pei(郭沛)[1], WU Shun-chuan(吴顺川)[1, 2]*, JIANG Ri-hua(姜日华)[3], ZHANG Guang(张光)[2]

1. Key Laboratory of Ministry of Education for Efficient Mining and Safety of Metal Mines (University of Science and Technology Beijing), Beijing 100083, China;
2. Faculty of Land Resource Engineering, Kunming University of Science and Technology, Kunming 650093, China;
3. School of Civil Engineering, Shandong University, Jinan 250061, China

Abstract: To explore the effects of thermal treatment on cracking processes in granite, granite samples were thermally treated at 25−400 ℃ and then loaded under uniaxial compression. Active ultrasonic testing and passive acoustic emission (AE) monitoring were combined to monitor the damage characteristics of the samples. The uniaxial compression strength (UCS) of the sample treated at 200 ℃ shows no apparent change compared with that of the nonheated sample, while the UCS increases at 300 °C and decreases at 400 ℃. As the temperature increases from 25 to 400 ℃, the initial P-wave velocity (V_p) decreases gradually from 4909 to 3823 m/s, and the initial V_p anisotropy ε increases slightly from 0.03 to 0.09. As the axial stress increases, ε increases rapidly in the crack closure stage and unstable cracking stage. The attenuation of ultrasonic amplitude spectra also shows an obvious anisotropy. Besides, the main location magnitude of AE events decreases after thermal treatment, and low-frequency AE events and high-amplitude AE events increasingly occur. However, there is insufficient evidence that the treatment temperature below 400 ℃ has a significant effect on the temporal characteristics, source locations, and *b*-values of AE.

Key words: uniaxial compression; thermal treatment; acoustic emission; ultrasonic; *b*-value; dominant frequency

Cite this article as: GUO Pei, WU Shun-chuan, JIANG Ri-hua, ZHANG Guang. Damage characteristics of thermally treated granite under uniaxial compression: Insights from active and passive ultrasonic techniques [J]. Journal of Central South University, 2022, 29(12): 4078−4093. DOI: https://doi.org/10.1007/s11771-022-5205-4.

1 Introduction

Granite is one of the most common rocks in the Earth's upper crust. This material is also commonly encountered at high-level radioactive waste (HLW) storage sites and in enhanced geothermal system (EGS) reservoirs [1−2]. Due to the difference in the thermal expansion coefficients and anisotropy of thermal expansion of mineral grains, thermally induced microcracks in rocks occur under high-temperature treatment [3 − 4]. An increase in thermally induced microcracks causes rock volume expansion, increases in porosity and permeability [5 − 7], and decreases in P-wave velocity (V_p), strength, and fracture toughness [8−9]. The effect of high temperatures can even change the mineral composition of rocks (especially the α-β quartz

Foundation item: Project(51934003) supported by the National Natural Science Foundation of China; China; Project(202105AE160023) supported by the Yunnan Innovation Team, China
Received date: 2022-03-25; **Accepted date:** 2022-07-01
Corresponding author: WU Shun-chuan, PhD, Professor; E-mail: wushunchuan@ustb.edu.cn; ORCID: https://orcid.org/0000-0001-6369-4896

transition at 573 ℃), which can drastically weaken rocks. High temperatures typically deteriorate the mechanical properties of rocks. However, mildly heated rock may be strengthened rather than weakened due to mineral expansion, the closure of initial pores, water evaporation, and the increasing textural complexity [10]. Changes in the rock microstructure at high temperatures significantly change the physical and mechanical properties of the rock, and 300 − 400 ℃ is considered to be the critical temperature range for thermal damage to granite [10 − 12]. Above this temperature, the physical and mechanical properties of granite change significantly [13 − 14]. In practical engineering, there are few cases in which granite can be exposed to temperatures higher than 400 ℃. For example, the reservoir temperature in EGS does not typically exceed 400 ° C at depths exceeding 3000 m [15]. Therefore, the changes in the physical and mechanical properties of granite below 400 ℃ are worthy of intensive study.

In laboratory tests, the acoustic emission (AE) monitoring technique is generally employed to study the initiation and propagation of cracks in brittle materials and has been widely used to evaluate various material damage states [16 − 18]. The temporal characteristics of AE can be used to indicate cracking activities [19] and determine stress thresholds [20 − 21]. The AE source location can indicate the location of cracking activities [22]. and AE frequency-amplitude characteristics [23−26] and *b*-values are considered precursors of rock failure [27 − 29]. AE characteristics have also been extensively studied to reveal the effect of high-temperature treatment on rock failure processes [30].

The active ultrasonic technique, which is commonly used in geophysics, is another ideal technique for identifying crack growth in rocks. GHAZVINIAN [31] used the ultrasonic velocity to identify the crack initiation threshold. SHIROLE et al [32] used four types of ultrasonic transducers with different dominant frequencies to study the evolution of the amplitude, frequency, and velocity of ultrasonic waves and noted that the changes in the amplitude and average frequency of ultrasonic waves can be used to characterize rock damage and identify crack initiation stress (σ_{ci}) and crack damage stress (σ_{cd}). With the development of ultrasonic methods in rock mechanics [32 − 33], the combination of passive AE monitoring and active ultrasonic testing has provided a reliable approach for assessing fracturing and the attenuation characteristics of rocks [24, 34−35].

To better understand the effects of thermal treatment on the damage evolution of granite samples, uniaxial compression tests were conducted, and active and passive ultrasonic techniques were employed in combination as monitoring methods. First, granite samples were heated to the target temperature (25, 200, 300 and 400 ℃) and were then slowly cooled to 25 ℃ to generate thermally induced microcracks. An axial load was then applied to the samples until failure. AE characteristics (e. g., temporal evolution, *b*-values, and amplitude-frequency characteristics of AE events), combined with ultrasonic characteristics (e. g., evolution of V_P in different ray paths, V_P anisotropy ε, and attenuation characteristics) were used to characterize the damage evolution of heated granite samples under uniaxial compression.

2 Experimental methods and procedures

2.1 Sample preparation

Granite samples were collected from Yanshan County, Jiangxi Province (northern Wuyi Mountain area in Southeast China), which is rich in mineral and geothermal resources [36]. The average density of the granite is 2.80 g/cm^3, and the porosity is 0.41%. X-ray diffraction (XRD) analysis of granite powder samples shows that the granite is composed of 51% feldspar, 32% biotite, 16% quartz, and a small amount of hornblende [23]. Cylindrical samples with a diameter of 40 mm and height of 80 mm were prepared using a hollow coring drill. The precision of the samples complies with ISRM recommendations [37]. We kept some samples at room temperature (25 ℃) and heated the remaining samples to 200, 300 and 400 ℃ using a KSL-1200X muffle furnace. To prevent thermal shock to the granite samples caused by rapid heating [38], the granite samples were heated at a constant rate of 5 ℃/min to the target temperature. After thermal treatment, each temperature was kept constant for 2 h to ensure thermal equilibrium in each sample. Finally, the samples were cooled naturally to room temperature (25 ℃) in the furnace, and the cooling

rate was less than the heating rate [39−40]. Table 1 lists the physical parameters of the granite samples before and after thermal treatment. The subscripts '1' and '2' for the length L, diameter D, and mass m indicate the values obtained before and after thermal treatment, respectively.

Table 1 Physical parameters of the granite samples before and after thermal treatment

No.	T/°C	L_1/ mm	L_2/ mm	D_1/ mm	D_2/ mm	m_1/g	m_2/g
G25	25	80.62	—	40.28	—	286.10	—
G200	200	80.52	80.55	40.27	40.28	285.80	285.60
G300	300	79.95	79.96	40.29	40.29	283.90	283.70
G400	400	80.57	80.63	40.19	40.22	284.70	284.40

2.2 Loading setup and procedure

In this study, the axial loading rate was 200 N/s, and a load of 40 kN was reached. Then a constant axial strain rate (2×10^{-6} s^{-1}) was maintained until the sample failed. A copper foil sheet (0.05 mm thick), a polytetra fluoroethylene sheet (0.05 mm thick) and MoS_2 smeared between them were selected as the antifriction materials. The copper foil was next to the sample surface to prevent the intrusion of MoS_2 [41]. One piezoelectric transducer was mounted in each sample holder, allowing V_P to be measured, as shown in Figure 1. Two axial linear variable differential transformers (LVDTs) and one lateral LVDT were attached to the sample to measure axial and lateral strains, respectively.

2.3 Active and passive ultrasonic monitoring

Active and passive ultrasonic techniques were used to study variations in V_P and AE during rock failure. As shown in Figure 1, eight piezoelectric transducers with diameters of 4 mm (PICO transducer made by PAC, resonant frequency of 500 kHz, operating frequency range of 200 − 750 kHz) were mounted using silicone grease on the sample, and two piezoelectric transducers (Nano30 transducer made by PAC; resonant frequency of 300 kHz and operating frequency range of 125 − 750 kHz) were mounted in sample holders to measure V_P in the axial direction. Two transducers mounted in sample holders were only used to measure V_P and not for AE source location.

As shown in Figure 1, the AE signals and

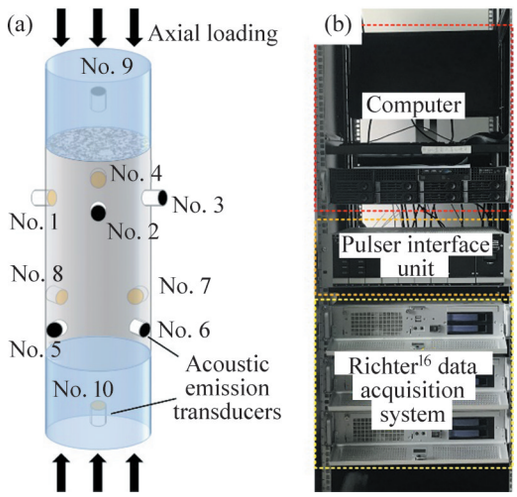

Figure 1 Schematic diagram of (a) axial loading and transducer array and (b) active and passive ultrasonic monitoring systems

pulser interface unit (PIU)-generated signals from the 10 transducers were preamplified by 50 dB (Channels 1, 3, 5, 7, 9, 10) and 30 dB (Channels 2, 4, 6 and 8) and then digitized at a sampling rate of 10 MHz with a sampling length of 1024 points (102.4 μs) for each event. Raw AE signals were bandpass filtered from 30 to 800 kHz. The analog-to-digital (A/D) system had a dynamic range of 16 bits. Continuous AE signals from ten channels were recorded by a Richter[16] continuous acquisition system and then on the hard disk of a PC.

The PIU can generate a 500 V pulse to each transducer to act as an active source for sequential V_P surveys, and the remaining nine transducers were used as receivers. One V_P survey was conducted before loading, and the surveys were conducted every minute during loading. In each V_P survey, the ultrasonic waves were stacked twice to improve the signal-to-noise ratio (SNR).

Eight transducers on the sample surface were used to continuously detect AE waveforms. Background noise was acquired at the beginning of the experiment to determine the trigger threshold. Since two gain values (50 dB and 30 dB) were used, two trigger thresholds (0.03 V and 0.01 V) were applied to trigger AE events, respectively. If the waveform amplitudes of four or more channels exceeded the thresholds within the time window (480 sample points), an AE event was recorded with a length of 1024 sample points. The P-wave arrival time of each waveform was automatically picked,

and the collapsing grid search algorithm was applied to locate AE events. A time-dependent transversely isotropic (TTI) velocity model [31] based on the 10-channel ultrasonic velocities was established for AE source location.

3 Results and analysis

3.1 Mechanical behavior

The stress − strain curves of granite samples treated at different temperatures are shown in Figure 2. The uniaxial compression strength (UCS) of granite samples treated at 200 ℃ showed little variation compared with that of samples treated at 25 ℃, and the UCS increased at 300 ℃ and then decreased at 400 ℃, which is consistent with the findings in previous studies [38, 42]. The peak axial strain shows a slight increase with increasing temperature, and all stress − strain curves illustrate typical nonlinear brittleness. The initial nonlinear deformation of the stress − strain curve at 400 ℃ is more significant than that of other curves due to the closure of preexisting microcracks, indicating the significant growth of thermally induced cracks from 300 to 400 ℃.

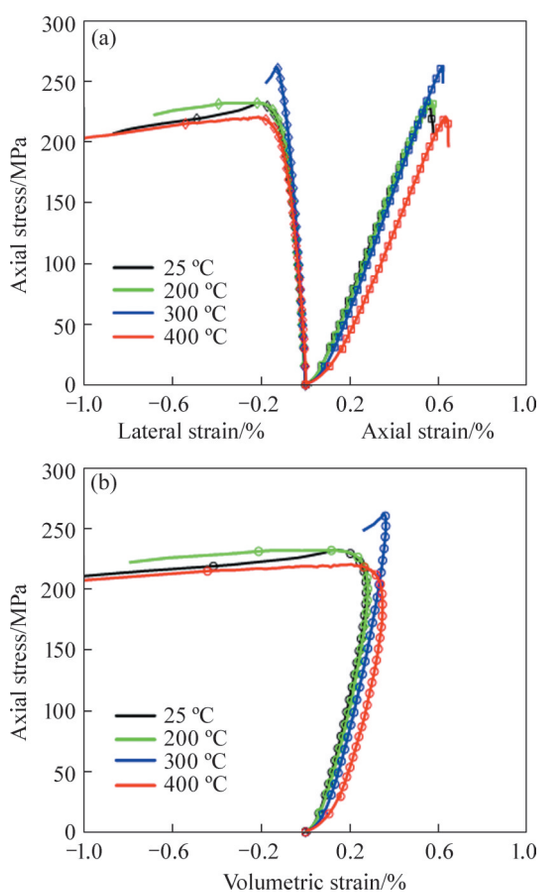

Figure 2 Stress−strain curves of the granite samples from uniaxial compression experiments: (a) Axial strain (square) and lateral strain (diamond); (b) Volumetric strain (circle)

There are several stress thresholds in the progressive failure process of brittle rocks, termed crack closure stress (σ_{cc}), σ_{ci}, σ_{cd} and UCS. Additionally, the progression of rock failure can be divided into four failure stages based on these stress thresholds: crack closure, elastic deformation, stable crack growth, and unstable cracking [43 − 45]. Table 2 shows the corresponding strength and deformation parameters of granite samples after thermal treatment. σ_{cd} was obtained from the maximum value of volumetric strain, and σ_{ci} and σ_{cc} were determined by the lateral strain response (LSR) method [46] and axial strain response (ASR) method [47], respectively. The strain-based stress thresholds of each sample are presented in Table 2. The σ_{cc}, σ_{ci} and σ_{cd} increased gradually before 300 ℃ and decreased at 400 ℃, which indicates that thermal treatment affects the stress thresholds as well. The elastic modulus (E) of granite was 47.62 GPa at 25 ℃, and E increased gradually to 47.96 GPa and 50.31 GPa for treatment temperatures of 200 and 300 ℃, respectively. E decreased to 46.72 GPa at 400 ℃, which is lower than that at 25 ℃. The stress threshold and E trends are consistent with the UCS trends; however, there is no apparent change in Poisson ratio (v).

Table 2 Strength and deformation parameters of granite samples after thermal treatment

No.	T/℃	σ_{cc}/ MPa	σ_{ci}/ MPa	σ_{cd}/ MPa	UCS/ MPa	v	E/ GPa
G25	25	31.01	127.18	198.06	232.51	0.21	47.62
G200	200	35.30	134.05	201.54	232.31	0.20	47.96
G300	300	39.91	163.52	257.01	261.93	0.21	50.31
G400	400	30.68	100.60	186.07	220.95	0.24	46.72

3.2 Characteristics of active and passive signals in different damage stages

Figure 3 presents the AE and V_P evolution trends during the uniaxial compression tests. In Figures 3(a) − (d), the axial stress, V_P values for different ray paths, AE rate, and cumulative AE for different temperatures are plotted versus time. The different colors of the dots represent the V_P values for different ray paths. The radial and axial

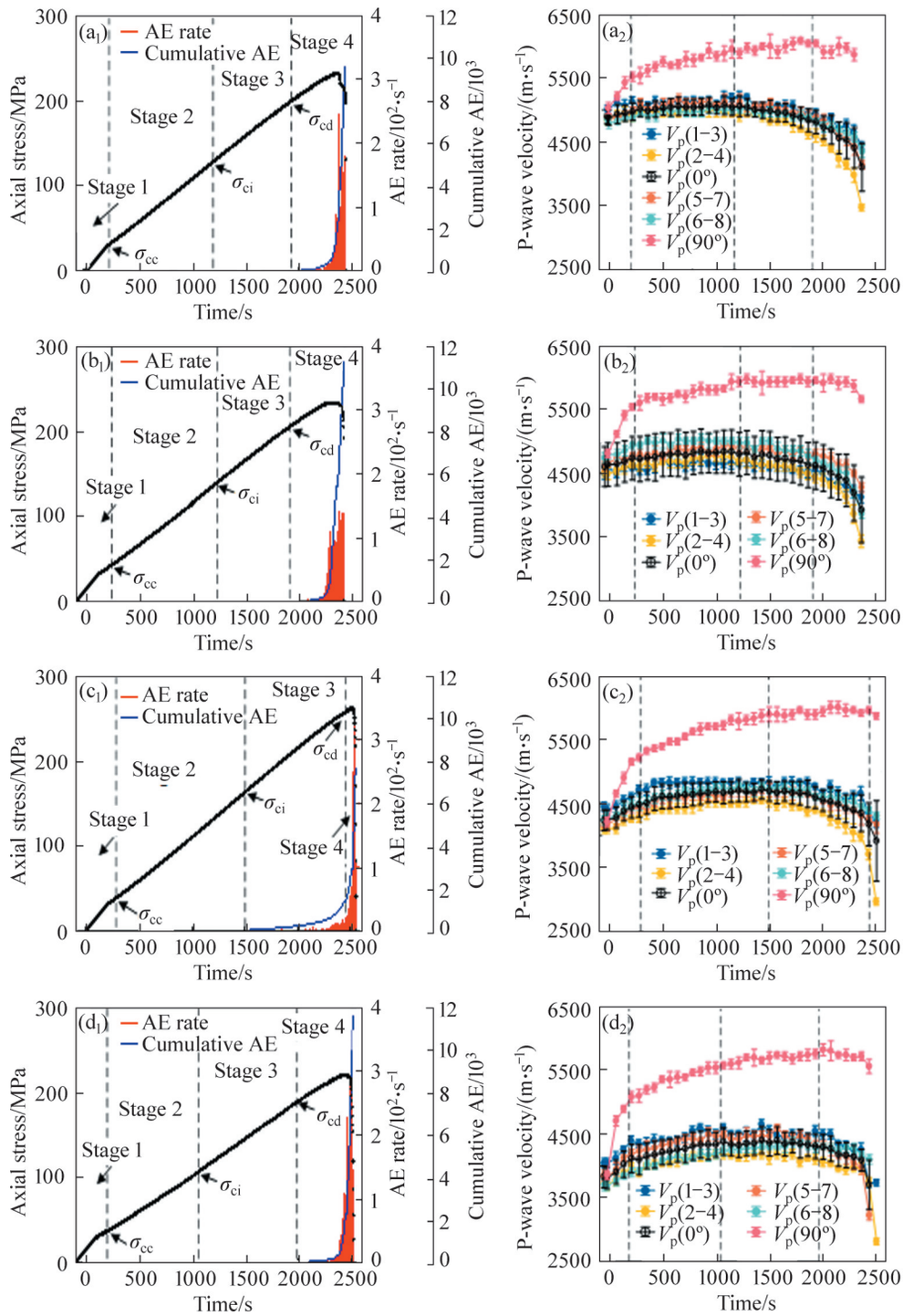

Figure 3 Evolution of AE and V_P under uniaxial compression at various temperatures: (a) 25 ℃; (b) 200 ℃; (c) 300 ℃; (d) 400 ℃

directions of the sample were defined as horizontal (0°) and vertical (90°). Four pairs of transducers were arranged face-to-face in the lateral direction of the samples, with ray paths 1−3, 2−4, 5−7 and 6−8. The V_P survey was performed with 1 kN preload and was then performed every minute during loading, with each survey lasting approximately 12 s. V_P was calculated based on the arrival time of the ultrasonic waveforms. Due to the presence of antifriction materials (copper sheet, polytetrafluoroethylene, and MoS_2), the vertical P-wave velocities could not be obtained before loading.

Based on the determined stress thresholds (σ_{cc}, σ_{ci} and σ_{cd}) shown in Table 2, the loading process

was defined as four stages (Stages 1 to 4). As shown in Figure 3, no AE event was detected in Stage 1. From the V_P survey with 1 kN preload, the mean P-wave velocities of samples treated at 25, 200, 300 and 400 °C were 4910, 4667, 4231 and 3823 m/s, respectively. With increasing axial stress, $V_P(90°)$ increased faster than $V_P(0°)$ in Stage 1. The rapid increase in $V_P(90°)$ can be explained by the closure of microcracks and micropores with increased axial stress. However, the predominantly vertical microcracks were rarely affected by the axial stress, which resulted in a smaller increase in $V_P(0°)$ than in $V_P(90°)$. In addition, due to the increase in thermally induced microcracks caused by thermal treatment, the growth rate of $V_P(90°)$ increased with the treatment temperature.

Once the internal cracks were closed, the samples displayed linear elastic deformation. In Stage 2, the first located AE event was triggered in all four tests, and only several AE events occurred in this stage. Compared to the trends observed in Stage 1, V_P increased more slowly, and $V_P(0°)$ reached a plateau. The plateau stage of $V_P(0°)$ in Figure 3 was also reported by LI et al [48], indicating a relative balance between preexisting crack closure and stress-induced crack initiation.

During the stable crack growth stage (Stage 3), the number of AE events increased from the initiation of microcracks to the beginning of volumetric strain reversal, indicating an increase in microfracture activity. $V_P(0°)$ decreased after the plateau period. $V_P(90°)$ increased slowly, and the fluctuation in $V_P(90°)$ before and after reaching the peak can be observed due to the competition between crack closure and opening.

In the stage from the initiation of unstable cracking to rock failure (Stage 4), the aggravation of crack nucleation, propagation, and coalescence led to a rapid increase in the number of AE events. Over 90% of the AE events were concentrated in this period, and the AE rate increased severely as the sample failed. The $V_P(0°)$ and $V_P(90°)$ results display a downward trend in this stage. The decline in $V_P(0°)$ is more obvious than that for $V_P(90°)$, which is caused by the Poisson effect under uniaxial stress. Additionally, in all tests, the V_P values measured in the ray path 2−4 direction decreased to the minimum because the macroscopic fractures of the samples were perpendicular to the direction of this ray path.

3.3 P-wave velocity anisotropy of active signals

Granite is typically considered to be homogeneous isotropic material. However, granite experiences stress-induced anisotropy under an external load. Thermally induced microcracks can enhance the anisotropy of granite [33, 49]. Since the closing and opening of microcracks can be affected by stress and thermal treatment, it is critical to quantitatively distinguish the anisotropy of granite caused by stress or thermal stress. Figure 4(a) shows the ultrasonic waveforms (ray path 2−4) for sample G25 during uniaxial loading. The transmission interval for adjacent surveys is 1 min. The wavelength of each ultrasonic waveform is 204.8 μs, and the amplitude is normalized. The colors of the waveforms change from blue to red, indicating the first survey to the last survey (survey

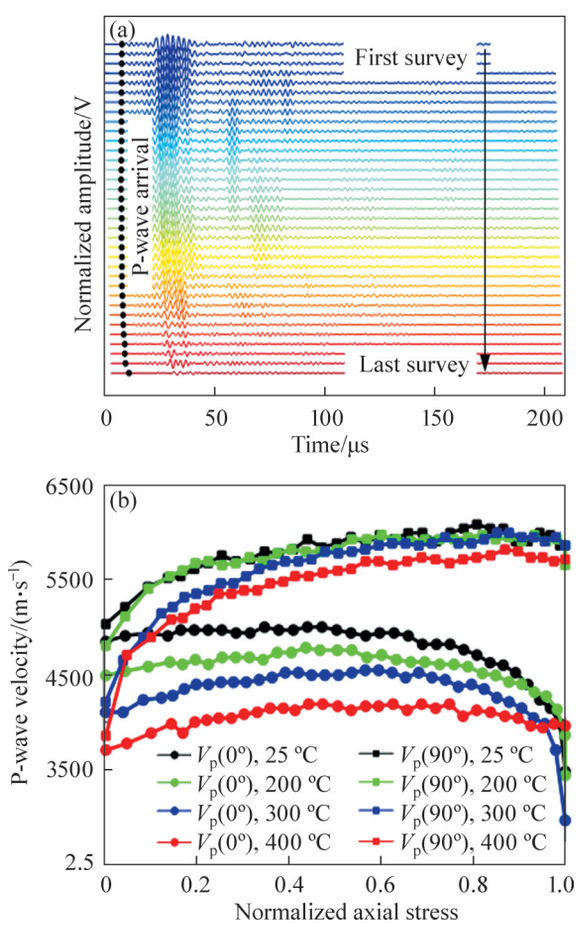

Figure 4 (a) The ultrasonic waveforms for ray path 2−4 during the uniaxial loading of sample G25; (b) The evolution of $V_P(90°)$ and $V_P(0°)$ during uniaxial compression experiments at various temperatures

1 to survey 35). Figure 4(b) shows the evolution of $V_P(90°)$ and $V_P(0°)$ during uniaxial loading. Both $V_P(90°)$ and $V_P(0°)$ decrease with the increase of the treatment temperature.

The parameter ε was proposed by THOMSEN [50] to characterize the V_P anisotropy and can be conveniently approximated as:

$$\varepsilon \approx \frac{V_P(90°) - V_P(0°)}{V_P(0°)} \tag{1}$$

where $V_P(90°)$ is the vertical P-wave velocity and $V_P(0°)$ is the horizontal P-wave velocity.

Figure 5 shows that the initial V_P anisotropy ε values of samples treated at 25, 200, 300 and 400 ℃ were 0.03, 0.05, 0.08 and 0.09, respectively. As the axial stress increased, ε increased rapidly until the axial stress reached σ_{cc}. The increase in ε growth rate is positively related to the temperature, which is due to the combined effect of the increased crack density and water escaping in thermally treated samples [51]. Because there was no confining pressure, microcracks parallel to the vertical direction could not be completely closed in the crack closure stage. Conversely, microcracks parallel to the horizontal direction were primarily closed. In other words, the difference in crack closure in different directions is the main reason for the variations in ε. The imbalance in V_P in different directions was magnified by thermal treatment. Thus, ε increased with the increase of treatment temperature.

As the axial stress exceeded σ_{cc}, ε slowly increased (Stage 2). In Stage 3, ε displayed a stable growth trend until the axial stress reached σ_{cd}. In Stage 4, ε increased rapidly. The maximum ε values

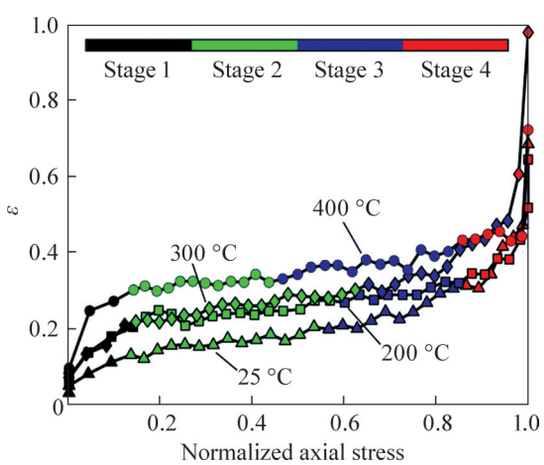

Figure 5 Evolution of V_P anisotropy ε at various temperatures

of samples treated at 25, 200, 300 and 400 ℃ were 0.69, 0.64, 0.98 and 0.72, respectively. Note that the final ε value at 400 ℃ was lower than that at 300 ℃. The probable reason is that the time interval of the V_P survey was 1 min; therefore, $V_P(0°)$ close to or at the failure point may not have been recorded.

In summary, the number of microcracks inside granite samples increases during thermal treatment, which leads to a slight increase in the initial ε. In addition, with increasing axial stress, the growth trend of ε exhibits good correspondence with crack growth processes. The increase in thermally induced microcracks contributes to an increase in the stress-induced ε.

3.4 Source locations of passive signals

Since the existence of thermally induced cracks increases the V_P anisotropy ε of the samples during uniaxial loading, it is important to adopt an appropriate velocity model based on the AE source location for rock samples with abundant cracks. We built the TTI velocity model to locate AE events based on the V_p values along different ray paths and reduce the location error of AE sources. Figures 6(a) – (d) show the source location of AE events and photographs of the failed samples. The sphere represents the AE event; the size and color of the sphere indicate the SNR and time from the beginning of the tests, respectively. Over 90% of the AE events occurred in Stage 4, and larger AE events occurred on the surface of the samples, which indicates that damage began at the sample surface due to spalling.

To investigate the effect of thermal treatment on the magnitude of AE events, the location magnitude M_L is defined as follows:

$$M_L = \lg\left(\frac{\sum_{m=1}^{n}(W_m \cdot d_m)}{n}\right) \tag{2}$$

where n is the number of transducers; d_m is the distance between the AE source location and the transducer; W_m is the amplitude of the waveform.

The location magnitudes M_L of AE events ranging from − 4.5 to − 1.5 were divided into 30 parts equally, and the proportions of all magnitudes were counted separately, as shown in Figure 6(e). AE events with magnitudes ranging from − 3.3 to

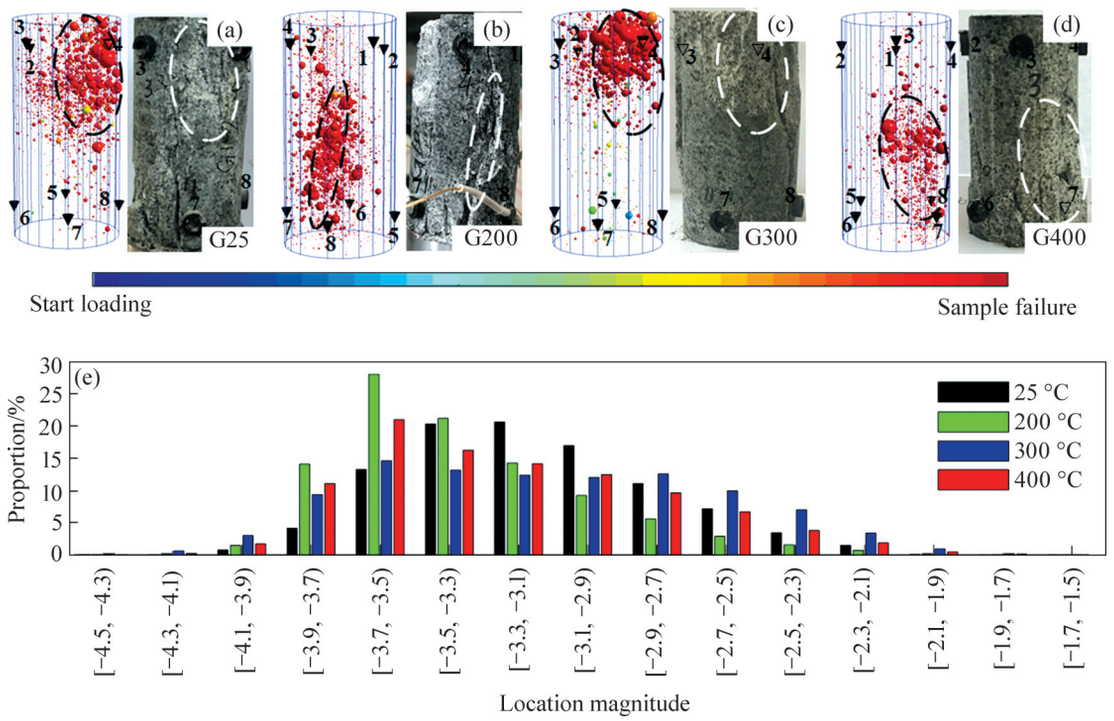

Figure 6 (a)−(d) Source locations of AE events and photographs of failed samples; (e) Magnitude statistics for AE events at different temperatures

−3.1 accounted for the largest proportion (20.71%) of all magnitudes at 25 °C. After thermal treatment at 200, 300 and 400 °C, AE events with amplitudes ranging from −3.7 to −3.3 accounted for the largest proportions, with values of 28.16%, 14.69% and 21.07%, respectively. The existence of thermally induced microcracks resulted in a reduction in the main location magnitude.

3.5 *b*-value analysis for passive signals

The magnitude distribution of natural earthquakes follows the Gutenberg-Richter (G-R) law [52]:

$$\lg N = a - bM \tag{3}$$

where M is the magnitude of earthquakes; N is the number of earthquake events with magnitudes greater than M; and a and b are constants. The G-R law can also be applied to assess the statistical results for AE events from laboratory experiments [27]. The parameter b, the so-called b-value, is an important precursor that reflects the fracturing processes of rocks [53]. In general, a low b-value indicates a larger proportion of high-magnitude AE events, and a high b-value indicates a larger proportion of low-magnitude AE events [54].

The location magnitude M_L was adopted as a simple estimation to calculate b-values in this paper [34], and we selected 0.05 as the magnitude interval. The time-dependent b-values were calculated by using the maximum likelihood estimation (MLE) method [55 − 56]. b-values were estimated using a running window of 1000 events and a step of 500 events.

Figure 7 shows the evolution characteristics of the AE rate and b-value for granite samples subjected to uniaxial compression. As shown in Figure 7(a), two stress drops occurred for sample G25. The first stress drop corresponds to a rapid decline in the b-value to 1.52, and the second stress drop corresponds to the final failure of the sample, where the b-value decreased to its minimum value of 1.41. Similar phenomena can be seen in Figures 7(b) − (d), and the decreased b-values correspond to the stress drops for each sample. The observed fluctuations in b-values are due to the unstable cracking process. The global minimum b-values of granite samples treated at 25, 200, 300 and 400 °C were 1.41, 1.37, 1.46 and 1.47, respectively. The effect of thermal treatment on the b-value cannot be observed due to the limited thermal damage below 400 °C.

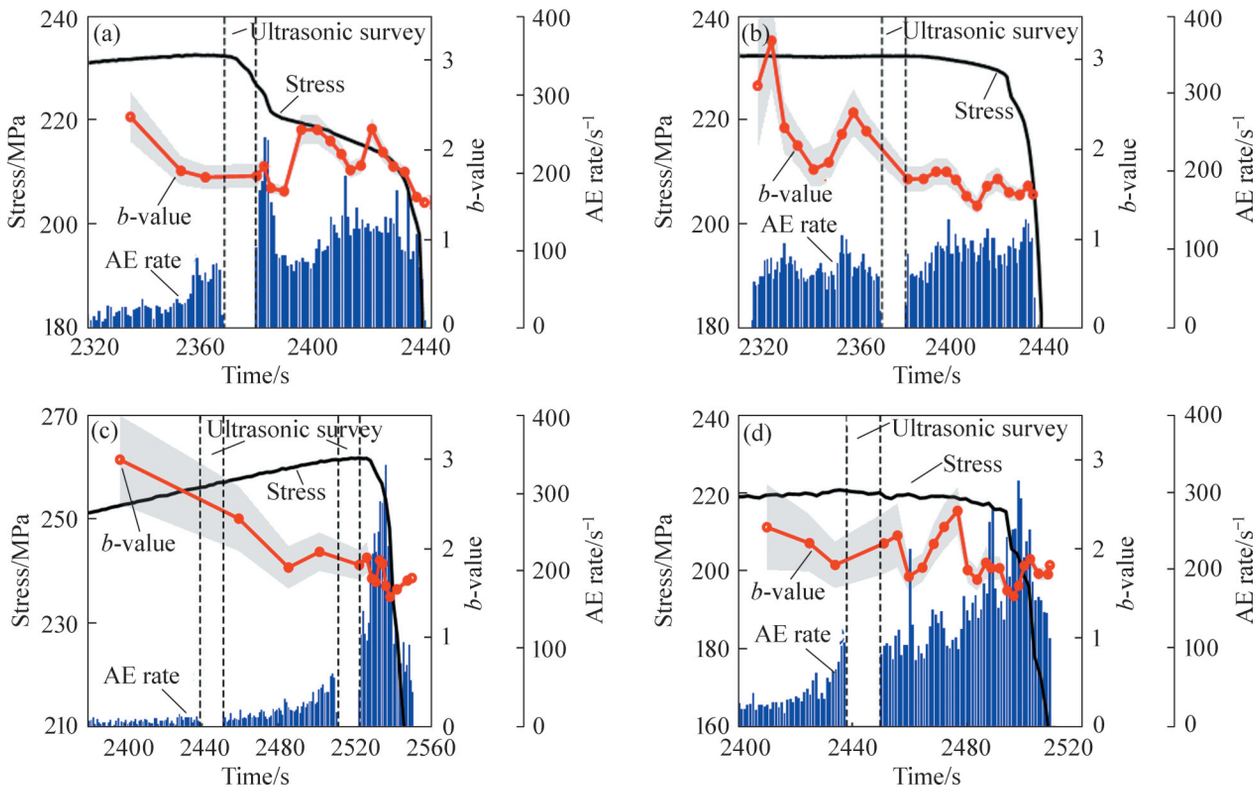

Figure 7 Stress, AE rate and *b*-value of granite samples during uniaxial loading at various treatment temperatures: (a) 25 ℃; (b) 200 ℃; (c) 300 ℃; (d) 400 ℃

3. 6 Spectral characteristics of active and passive signals

Vertical (90°) ultrasonic waves (ray path 9−10) and horizontal (0°) ultrasonic waves (ray path 2−4) recorded during the uniaxial compression tests were adopted for amplitude spectrum analysis to evaluate the cracking process. In this study, 100 sample points (10 μs) for each ultrasonic waveform were sectioned by using a Hanning window. The amplitude spectrum was calculated using fast Fourier transform (FFT). The relative changes in different directions in attenuation were investigated.

As shown in Figure 8, the dominant frequency of vertical (90°) ultrasonic waves was approximately 300 kHz, and the dominant frequency of horizontal (0°) ultrasonic waves was approximately 500 kHz. The differences in the dominant frequency are primarily due to the different types of transducers used.

Figures 8(a)−(d) show that the amplitude of the dominant frequency of vertical ultrasonic waveforms increases with increasing stress level, especially from the beginning of tests to σ_{cc}, where axial compaction is the main influential mechanism [24]. As depicted in Figures 8(e)−(h), the amplitude spectrum of the horizontal ultrasonic waveforms attenuates from the beginning of loading to rock failure. The slight increase in $V_p(0°)$ in the initial stage does not significantly increase the ultrasonic amplitude.

Next, the FFT algorithm was adopted to calculate the dominant frequency of AE signals. Figure 9 shows that the dominant frequency of AE signals was mainly distributed in the range of 400−600 kHz with small amplitudes in the initial stage of loading. The amplitudes of AE events increased with increasing loading level, and a small number of high-frequency and a large number of low-frequency AE events occurred in the final loading stage. As the temperature increased, the high-frequency signals decreased, while the low-frequency signals increased, which reflects the obvious impact of thermal treatment on the AE frequency features.

4 Discussion

Previous studies have shown a positive

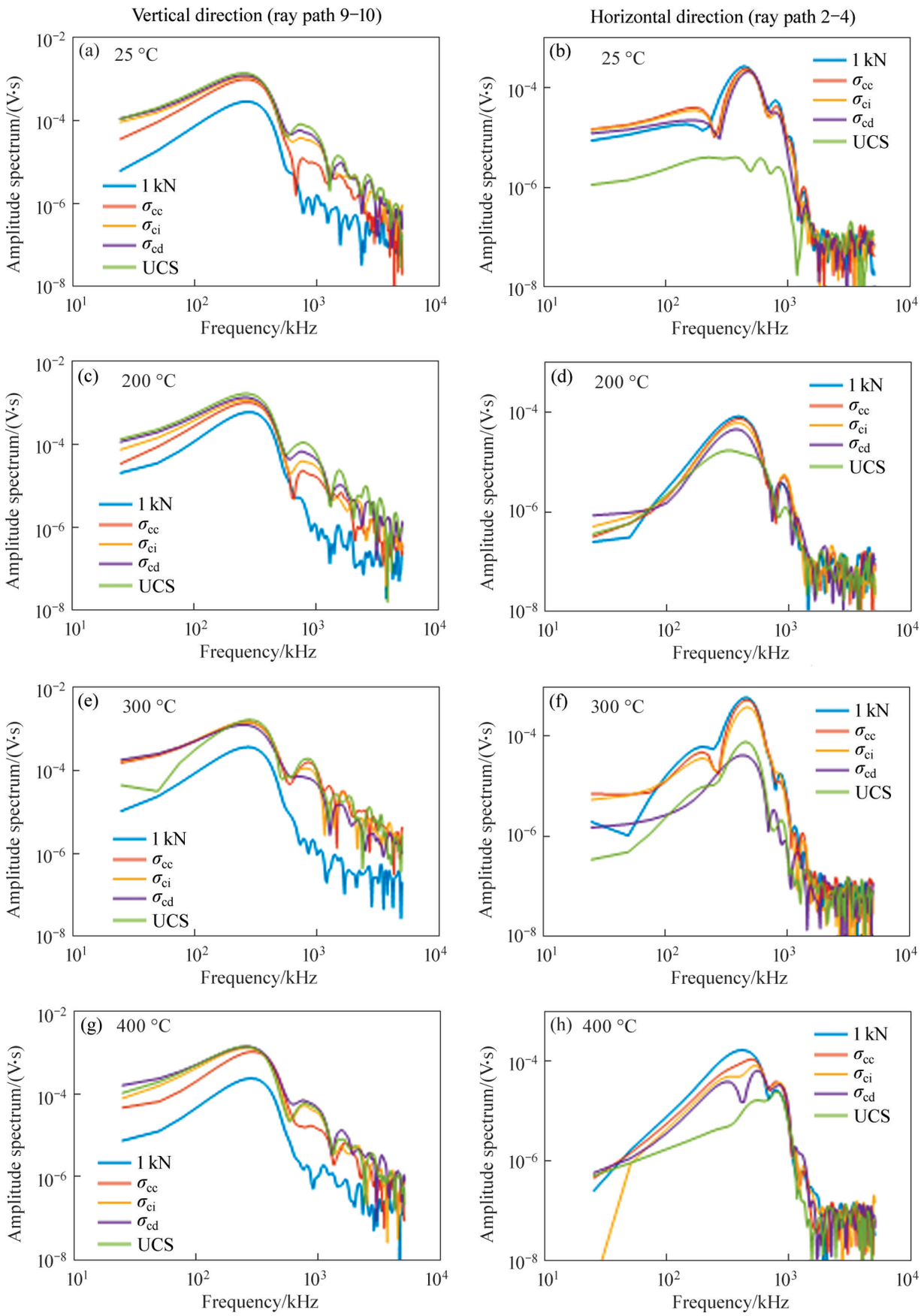

Figure 8 Spectral amplitudes of ultrasonic waveforms at different stress levels (1 kN, σ_{cc}, σ_{ci}, σ_{cd}, and UCS) and temperatures: (a, b) 25 °C; (c, d) 200 °C; (e, f) 300 °C; (e, h) 400 °C

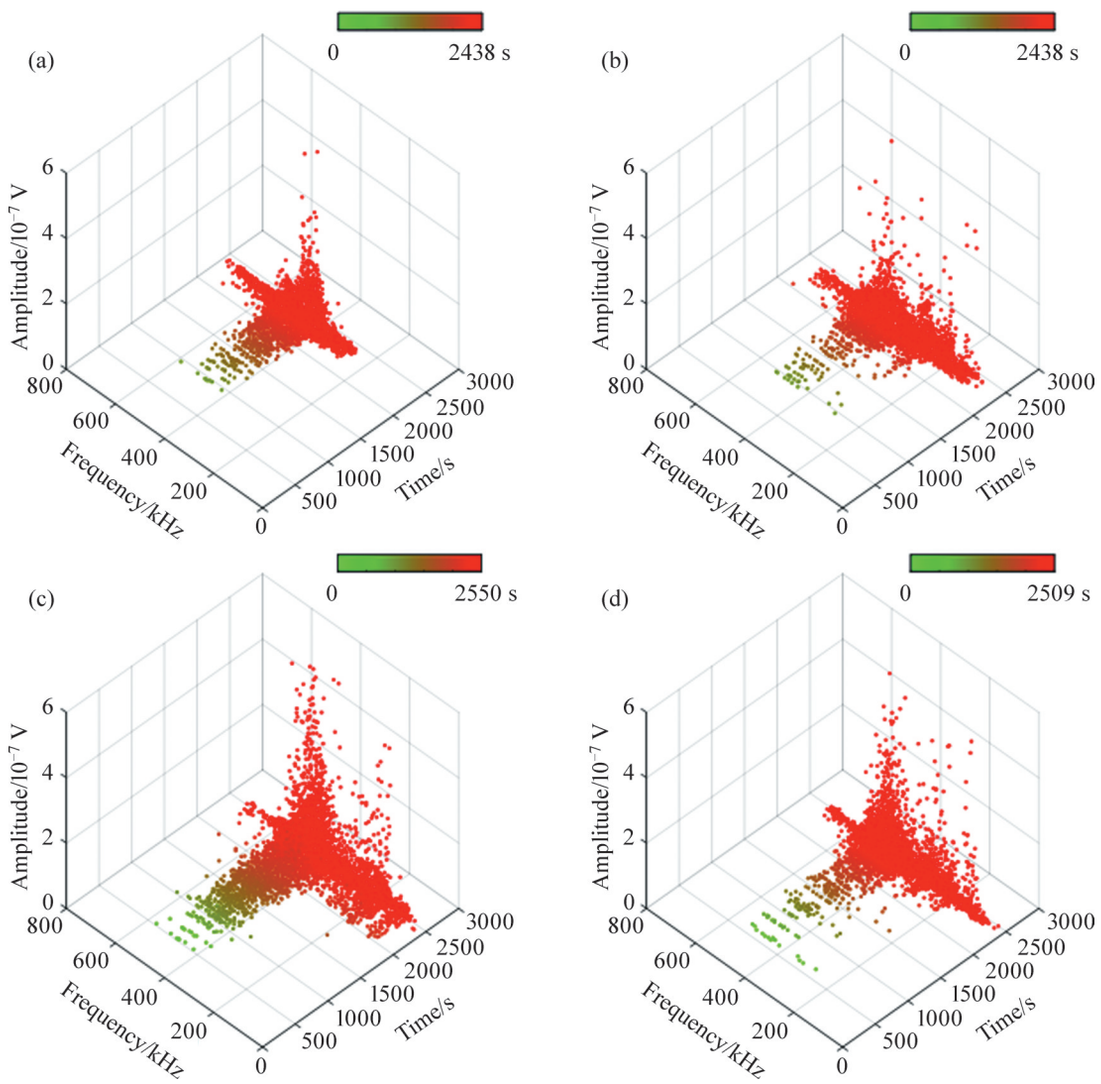

Figure 9 Amplitude-frequency characteristics of AE events under uniaxial compression: (a) 25 ℃; (b) 200 ℃; (c) 300 ℃; (d) 400 ℃

correlation between the UCS and V_P values of rocks at room temperature, and various empirical equations have been developed to simply estimate the UCS of rocks by using V_P [57 − 58]. ZHANG et al [59] found inconsistencies in the changes in UCS and V_P in sandstone after thermal treatment based on a study of 18 kinds of sandstones. In this study, it also was found that with the increasing temperature, V_P decreased monotonically, but UCS increased first and then decreased. To verify whether this inconsistency is a common phenomenon for granite, the UCS and V_P values of granite after high-temperature treatment were recorded and normalized (the UCS and V_P values at various temperatures divided by those at room temperature, respectively) as shown in Figure 10.

The granite samples shown in Figure 10 all experienced slow heating (≤5 ℃), temperature maintenance and cooling (rapid or slow cooling). There are two UCS trends with increasing temperature, and V_P decreases monotonically. Furthermore, the relationship between V_P and UCS is plotted in Figure 11, and granite is divided into type I (UCS decreases monotonically and V_P decreases) and type II (UCS increases first and then decreases, and V_P decreases).

A series of physical and chemical reactions will occur as rocks undergo high-temperature treatment. At the target temperature (up to 400 ℃) in this study, chemical changes (e. g., quartz $\alpha-\beta$ transformation at 573 ℃) are unlikely to occur [10−11, 51], and the changes in physical characteristics

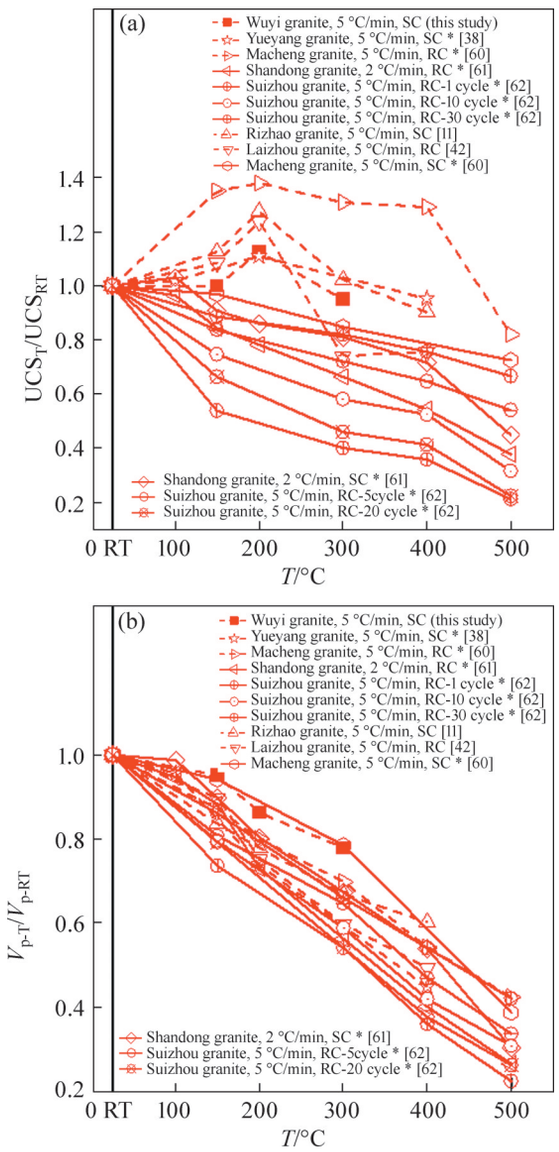

Figure 10 UCS and V_p values of granite after high temperature treatment (RT denotes room temperature of 20 – 25 °C; SC and RC denote slow cooling and rapid cooling, respectively; * means average value; different cycles for Suizhou granite samples denote the numbers of heating and rapid cooling cycles)

(e.g., water loss, mass loss, and cracking activities) are the main changes for granite. The temperature ranges from 25 to 400 °C can be divided into three phases to better understand the mechanisms of the thermal effect on granite.

Phase I (25–200 °C): The thermal expansion of mineral grains results in a slight reduction or the closure of preexisting cracks inside the granite, which leads to improved strength [11]. Thermally induced microcracks are generated and thus decrease the strength of the granite [14]. The escape

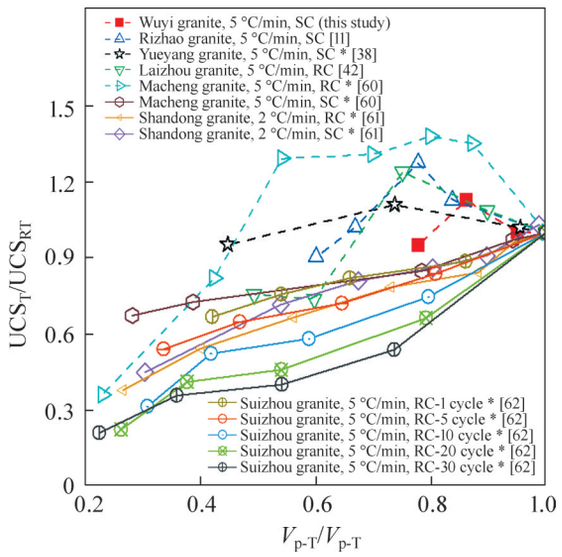

Figure 11 Relationship between the P-wave velocity and UCS of granite after high temperature treatment (The solid and dashed lines denote type I and type II granite, respectively; * means average value)

of absorbed water at 100 – 110 °C temporarily increases the effective stress and strength of granite [12, 63]. The UCS of granite does not change significantly due to the aforementioned competition among these mechanisms as the temperature increases from 25 to 200 °C.

Phase II (200–300 °C): The preexisting cracks close due to thermal expansion, thermally induced microcracks increase, and bound water escapes [51]. The strengthening effect of water escape on UCS is greater than the weakening effect of the increase in thermally induced microcracks, resulting in an increase in UCS.

Phase III (300 – 400 °C): The increase in thermally induced microcracks enhances cracking activities. Structural water and crystal water escape, which results in damage to the crystal mineral structure [12]. UCS thus decreases as the treatment temperature increase from 300 to 400 °C. The temperature range of 300 – 400 °C is an important threshold for assessing the thermal damage of granite, as noted in Refs. [12, 42, 64].

The Wuyi granite analyzed in this study is a type II granite. Specifically, as the temperature increased from 25 to 200 °C, UCS did not change significantly, even with the competition among the aforementioned mechanisms. In the range of 200 – 300 °C, the strengthening effect of water escape on

UCS was greater than the weakening effect of the increase in thermally induced microcracks, resulting in an increase in UCS. The UCS at 400 ℃ decreased below room temperature, indicating that the weakening effect of thermally induced microcracks is dominant.

The characteristics of active ultrasound and AE are closely related to these mechanisms. The increase in thermally induced microcracks and the escape of water inside the granite lead to a gradual decline in V_p with increasing temperature. During the loading process, the combined action of thermally induced cracks and stress-induced cracks increases ε, the proportion of small-magnitude AE events increases, and the proportion of low-frequency AE events increases. The *b*-value does not display an apparent change, likely because the thermal treatment below 400 ℃ does not change the brittle behavior of the granite samples.

5 Conclusions

In this study, active ultrasonic and passive AE techniques were adopted to study the fracturing processes of thermally treated granite under uniaxial compression. The V_p, ε, and spectral characteristics of ultrasonic waves were studied by active ultrasonic monitoring. The temporal evolution of AE events, *b*-values, and amplitude-frequency characteristics were studied by passive AE monitoring. The detailed conclusions are as follows:

1) Ultrasonic waves are more sensitive to subtle changes in granite after thermal treatment than before treatment. Although the UCS of granite is almost unchanged after the 200 ℃ treatment, the initial V_p decreases from 4909 to 4667 m/s. In addition, the initial anisotropy ε increases slightly from 0.03 to 0.05. After the 300 and 400 ℃ treatments, the UCS is 112.65% and 95.03% of the UCS at 25 ℃, respectively. Additionally, the initial V_p decreases to 4231 and 3823 m/s, respectively, and the initial anisotropy ε increases to 0.08 and 0.09, respectively.

2) The granites treated at temperatures below 400 ℃ display obvious brittle characteristics. The main location magnitude of AE events decreases from [−3.3− −3.1] to [−3.7− −3.5]. The amplitude−frequency characteristics of AE events indicate that low-frequency AE events and high-amplitude AE events increase with increasing temperature. However, it is difficult to observe apparent thermal effects for temporal characteristics, source locations, and time-dependent *b*-values for AE events.

3) Axial stress influences the development of stress-induced microcracks, and the combined action of preexisting cracks (including thermally induced cracks) and stress-induced cracks leads to changes in ultrasonic and AE features. With increasing axial stress, V_p (90°) and V_p (0°) first increase and then decrease. The anisotropy ε also exhibits different modes (rapid increase, stable increase, and rapid increase again) of increase at different loading stages due to crack closing and opening under axial stress.

4) The amplitude of the dominant frequency of vertical ultrasonic waves increases with the increasing stress level, and the amplitude of the dominant frequency of horizontal ultrasonic waves attenuates due to cracking along the axial axis.

We conducted uniaxial compression tests, which represent the stress state of rock masses such as mine pillars in practical engineering. Since an engineering rock mass is generally under triaxial stress conditions, our next objective is to use ultrasonic and AE monitoring techniques to study the corresponding rock fracturing and instability precursors under triaxial conditions.

Contributors

GUO Pei provided the concept and wrote the first draft of the manuscript. WU Shun-chuan supervised the work and edited the draft of the manuscript. JIANG Ri-hua and ZHANG Guang analyzed the measured data.

Conflict of interest

GUO Pei, WU Shun-chuan, JIANG Ri-hua, ZHANG Guang declare that they have no conflict of interest.

References

[1] WANG Ju, CHEN Liang, SU Rui, et al. The Beishan underground research laboratory for geological disposal of high-level radioactive waste in China: Planning, site selection, site characterization and in situ tests [J]. Journal of Rock Mechanics and Geotechnical Engineering, 2018, 10(3): 411−435. DOI: 10.1016/j.jrmge.2018.03.002.

[2] LU S M. A global review of enhanced geothermal system

(EGS) [J]. Renewable and Sustainable Energy Reviews, 2018, 81: 2902−2921. DOI: 10.1016/j.rser.2017.06.097.

[3] FREDRICH J T, WONG T F. Micromechanics of thermally induced cracking in three crustal rocks [J]. Journal of Geophysical Research: Solid Earth, 1986, 91(B12): 12743 − 12764. DOI: 10.1029/jb091ib12p12743.

[4] YIN Tu-bing, LI Xi-bing, CAO Wen-zhuo, et al. Effects of thermal treatment on tensile strength of laurentian granite using Brazilian test [J]. Rock Mechanics and Rock Engineering, 2015, 48(6): 2213−2223. DOI: 10.1007/s00603-015-0712-3.

[5] CHAKI S, TAKARLI M, AGBODJAN W P. Influence of thermal damage on physical properties of a granite rock: Porosity, permeability and ultrasonic wave evolutions [J]. Construction and Building Materials, 2008, 22(7): 1456 − 1461. DOI: 10.1016/j.conbuildmat.2007.04.002.

[6] CHEN Shi-wan, YANG Chun-he, WANG Gui-bin. Evolution of thermal damage and permeability of Beishan granite [J]. Applied Thermal Engineering, 2017, 110: 1533 − 1542. DOI: 10.1016/j.applthermaleng.2016.09.075.

[7] ZHANG Wei-qiang, SUN Qiang, ZHANG Yu-liang, et al. Porosity and wave velocity evolution of granite after high-temperature treatment: A review [J]. Environmental Earth Sciences, 2018, 77(9): 1 − 13. DOI: 10.1007/s12665-018-7514-3.

[8] WU Shun-chuan, GUO Pei, ZHANG Shi-huai, et al. Study on thermal damage of granite based on Brazilian splitting test [J]. Chinese Journal of Rock Mechanics and Engineering, 2018(S2): 3805−3816. (in Chinese)

[9] NASSERI M H B, TATONE B S A, GRASSELLI G, et al. Fracture toughness and fracture roughness interrelationship in thermally treated westerly granite [J]. Pure and Applied Geophysics, 2009, 166(5 − 7): 801 − 822. DOI: 10.1007/s00024-009-0476-3.

[10] WONG L N Y, ZHANG Ya-hui, WU Zhi-jun. Rock strengthening or weakening upon heating in the mild temperature range? [J]. Engineering Geology, 2020, 272: 105619. DOI: 10.1016/j.enggeo.2020.105619.

[11] YANG Sheng-qi, RANJITH P G, JING Hong-wen, et al. An experimental investigation on thermal damage and failure mechanical behavior of granite after exposure to different high temperature treatments [J]. Geothermics, 2017, 65: 180−197. DOI: 10.1016/j.geothermics.2016.09.008.

[12] SUN Qiang, ZHANG Wei-qiang, XUE Lei, et al. Thermal damage pattern and thresholds of granite [J]. Environmental Earth Sciences, 2015, 74(3): 2341 − 2349. DOI: 10.1007/s12665-015-4234-9.

[13] XU Xiao-li, KARAKUS M, GAO Feng, et al. Thermal damage constitutive model for rock considering damage threshold and residual strength [J]. Journal of Central South University, 2018, 25(10): 2523−2536. DOI: 10.1007/s11771-018-3933-2.

[14] ZUO Jian-ping, WANG Jin-tao, SUN Yun-jiang, et al. Effects of thermal treatment on fracture characteristics of granite from Beishan, a possible high-level radioactive waste disposal site in China [J]. Engineering Fracture Mechanics, 2017, 182: 425 − 437. DOI: 10.1016/j.engfracmech. 2017. 04.043.

[15] BERTANI R. World geothermal power generation in the period 2001 − 2005 [J]. Geothermics, 2005, 34(6): 651 − 690. DOI: 10.1016/j.geothermics.2005.09.005.

[16] LEI Xing-lin, MA Sheng-li. Laboratory acoustic emission study for earthquake generation process [J]. Earthquake Science, 2014, 27(6): 627 − 646. DOI: 10.1007/s11589-014-0103-y.

[17] LOCKNER D. The role of acoustic emission in the study of rock fracture [J]. International Journal of Rock Mechanics and Mining Sciences & Geomechanics Abstracts, 1993, 30(7): 883−899. DOI: 10.1016/0148-9062(93)90041-B.

[18] SU Guo-shao, GAN Wei, ZHAI Shao-bin, et al. Acoustic emission precursors of static and dynamic instability for coarse-grained hard rock [J]. Journal of Central South University, 2020, 27(10): 2883−2898. DOI: 10.1007/s11771-020-4516-6.

[19] ZHANG Jian-zhi, ZHOU Xiao-ping. AE event rate characteristics of flawed granite: From damage stress to ultimate failure [J]. Geophysical Journal International, 2020, 222(2): 795−814. DOI: 10.1093/gji/ggaa207.

[20] ZHAO X G, CAI M, WANG J, et al. Objective determination of crack initiation stress of brittle rocks under compression using AE measurement [J]. Rock Mechanics and Rock Engineering, 2015, 48(6): 2473−2484. DOI: 10.1007/s00603-014-0703-9.

[21] WU Chen, GONG Feng-qiang, LUO Yong. A new quantitative method to identify the crack damage stress of rock using AE detection parameters [J]. Bulletin of Engineering Geology and the Environment, 2021, 80(1): 519−531. DOI: 10.1007/s10064-020-01932-6.

[22] DONG Long-jun, HU Qing-chun, TONG Xiao-jie, et al. Velocity-free MS/AE source location method for three-dimensional hole-containing structures [J]. Engineering, 2020, 6(7): 827−834. DOI: 10.1016/j.eng.2019.12.016.

[23] GUO Pei, WU Shun-chuan, ZHANG Guang, et al. Effects of thermally-induced cracks on acoustic emission characteristics of granite under tensile conditions [J]. International Journal of Rock Mechanics and Mining Sciences, 2021, 144: 104820. DOI: 10.1016/j.ijrmms.2021.104820.

[24] GOODFELLOW S D, TISATO N, GHOFRANITABARI M, et al. Attenuation properties of Fontainebleau sandstone during true-triaxial deformation using active and passive ultrasonics [J]. Rock Mechanics and Rock Engineering, 2015, 48(6): 2551−2566. DOI: 10.1007/s00603-015-0833-8.

[25] OHNAKA M, MOGI K. Frequency characteristics of acoustic emission in rocks under uniaxial compression and its relation to the fracturing process to failure [J]. Journal of Geophysical Research, 1982, 87: 3873−3884. DOI: 10.1029/JB087IB05P03873.

[26] LI L R, DENG J H, ZHENG L, et al. Dominant frequency characteristics of acoustic emissions in white marble during direct tensile tests [J]. Rock Mechanics and Rock Engineering, 2017, 50(5): 1337−1346. DOI: 10.1007/s00603-016-1162-2.

[27] AMITRANO D. Brittle-ductile transition and associated seismicity: Experimental and numerical studies and relationship with the *b* value [J]. Journal of Geophysical Research: Solid Earth, 2003, 108(B1): 2044. DOI: 10.1029/2001jb000680.

[28] LIU Xi-ling, HAN Meng-si, HE Wei, et al. A new *b* value estimation method in rock acoustic emission testing [J]. Journal of Geophysical Research: Solid Earth, 2020, 125(12): e2020JB019658. DOI: 10.1029/2020jb019658.

[29] CHEN Dao-long, LIU Xi-ling, HE Wei, et al. Effect of attenuation on amplitude distribution and b value in rock acoustic emission tests [J]. Geophysical Journal International, 2021, 229(2): 933 − 947. DOI: 10.1093/gji/ggab480.

[30] SHAO Shi-shi, RANJITH P G, WASANTHA P L P, et al. Experimental and numerical studies on the mechanical behaviour of Australian Strathbogie granite at high temperatures: An application to geothermal energy [J]. Geothermics, 2015, 54: 96 − 108. DOI: 10.1016/j.geothermics.2014.11.005.

[31] GHAZVINIAN E. Fracture initiation and propagation in low porosity crystalline rocks: Implications for excavation damage zone (EDZ) mechanics [D]. Kingston, Canada: Queen's University, 2015.

[32] SHIROLE D, HEDAYAT A, GHAZANFARI E, et al. Evaluation of an ultrasonic method for damage characterization of brittle rocks [J]. Rock Mechanics and Rock Engineering, 2020, 53(5): 2077 − 2094. DOI: 10.1007/s00603-020-02045-y.

[33] WANG Xiao-qiong, SCHUBNEL A, FORTIN J, et al. Physical properties and brittle strength of thermally cracked granite under confinement [J]. Journal of Geophysical Research: Solid Earth, 2013, 118(12): 6099 − 6112. DOI: 10.1002/2013jb010340.

[34] ZHANG Shi-huai, WU Shun-chuan, ZHANG Guang, et al. Three-dimensional evolution of damage in sandstone Brazilian discs by the concurrent use of active and passive ultrasonic techniques [J]. Acta Geotechnica, 2020, 15(2): 393−408. DOI: 10.1007/s11440-018-0737-3.

[35] STANCHITS S, VINCIGUERRA S, DRESEN G. Ultrasonic velocities, acoustic emission characteristics and crack damage of basalt and granite [J]. Pure and Applied Geophysics, 2006, 163(5 − 6): 975 − 994. DOI: 10.1007/s00024-006-0059-5.

[36] XIONG Liang-feng, WU Shun-chuan, ZHANG Shi-huai. Mechanical behavior of a granite from Wuyi Mountain: Insights from strain-based approaches [J]. Rock Mechanics and Rock Engineering, 2019, 52(3): 719−736. DOI: 10.1007/s00603-018-1617-8.

[37] FAIRHURST C, HUDSON J. Draft ISRM suggested method for the complete stress-strain curve for intact rock in uniaxial compression [J]. International Journal of Rock Mechanics and Mining Sciences, 1999, 36: 279−289.

[38] XU Lei, GONG Feng-qiang, LIU Zhi-xiang. Experiments on rockburst proneness of pre-heated granite at different temperatures: Insights from energy storage, dissipation and surplus [J]. Journal of Rock Mechanics and Geotechnical Engineering, 2022, 14(5): 1343−1355. DOI: 10.1016/j.jrmge.2021.08.004.

[39] YIN Tu-bing, TAN Xiao-song, WU You, et al. Temperature dependences and rate effects on Mode II fracture toughness determined by punch-through shear technique for granite [J]. Theoretical and Applied Fracture Mechanics, 2021, 114: 103029. DOI: 10.1016/j.tafmec.2021.103029.

[40] LI Xiang, HUANG Si, YIN Tu-bing, et al. Dynamic properties of thermal shock treated sandstone subjected to coupled dynamic and static loads [J]. Minerals, 2021, 11(8): 889. DOI: 10.3390/min11080889.

[41] ZHANG Shi-huai, WU Shun-chuan, CHU Chao-qun, et al. Acoustic emission associated with self-sustaining failure in low-porosity sandstone under uniaxial compression [J]. Rock Mechanics and Rock Engineering, 2019, 52(7): 2067−2085. DOI: 10.1007/s00603-018-1686-8.

[42] LI Ning, MA Xin-fang, ZHANG Shi-cheng, et al. Thermal effects on the physical and mechanical properties and fracture initiation of Laizhou granite during hydraulic fracturing [J]. Rock Mechanics and Rock Engineering, 2020, 53(6): 2539−2556. DOI: 10.1007/s00603-020-02082-7.

[43] BRACE W F, PAULDING B W, SCHOLZ C. Dilatancy in the fracture of crystalline rocks [J]. Journal of Geophysical Research Atmospheres, 1966, 71(16): 3939 − 3953. DOI: 10.1029/jz071i016p03939.

[44] CAI M, KAISER P K, TASAKA Y, et al. Generalized crack initiation and crack damage stress thresholds of brittle rock masses near underground excavations [J]. International Journal of Rock Mechanics and Mining Sciences, 2004, 41(5): 833−847. DOI: 10.1016/j.ijrmms.2004.02.001.

[45] MARTIN C D, CHANDLER N A. The progressive fracture of Lac du Bonnet granite [J]. International Journal of Rock Mechanics and Mining Sciences & Geomechanics Abstracts, 1994, 31(6): 643−659. DOI: 10.1016/0148-9062(94)90005-1.

[46] NICKSIAR M, MARTIN C D. Evaluation of methods for determining crack initiation in compression tests on low-porosity rocks [J]. Rock Mechanics and Rock Engineering, 2012, 45(4): 607−617. DOI: 10.1007/s00603-012-0221-6.

[47] PENG Jun, CAI Ming, RONG Guan, et al. Stresses for crack closure and its application to assessing stress-induced microcrack damage [J]. Journal of Rock Mechanics and Engineering, 2015, 34(6): 1091−1100. DOI: 10.13722/j.cnki.jrme.2014.1151. (in Chinese)

[48] LI Zhi, FORTIN J, NICOLAS A, et al. Physical and mechanical properties of thermally cracked andesite under pressure [J]. Rock Mechanics and Rock Engineering, 2019, 52(10): 3509−3529. DOI: 10.1007/s00603-019-01785-w.

[49] DAVID C, MENÉNDEZ B, DAROT M. Influence of stress-induced and thermal cracking on physical properties and microstructure of La Peyratte granite [J]. International Journal of Rock Mechanics and Mining Sciences, 1999, 36(4): 433−448. DOI: 10.1016/S0148-9062(99)00010-8.

[50] THOMSEN L. Weak elastic anisotropy [J]. Geophysics, 1986, 51(10): 1954−1966. DOI: 10.1190/1.1442051.

[51] ZHANG Wei-qiang, SUN Qiang, HAO Shu-qing, et al. Experimental study on the variation of physical and mechanical properties of rock after high temperature treatment [J]. Applied Thermal Engineering, 2016, 98: 1297−1304. DOI: 10.1016/j.applthermaleng.2016.01.010.

[52] GUTENBERG B, RICHTER C F. Frequency of earthquakes in California [J]. Bulletin of the Seismological Society of America, 1944, 34(4): 185 − 188. DOI: 10.1785/bssa0340040185.

[53] SCHOLZ C H. The frequency-magnitude relation of microfracturing in rock and its relation to earthquakes [J]. Bulletin of the Seismological Society of America, 1968,

58(1): 399−415. DOI: 10.1785/bssa0580010399.
[54] COLOMBO I S, MAIN I G, FORDE M C. Assessing damage of reinforced concrete beam using "*b*-value" analysis of acoustic emission signals [J]. Journal of Materials in Civil Engineering, 2003, 15(3): 280−286. DOI: 10.1061/(asce)0899-1561(2003)15: 3(280).
[55] AKI K. Maximum likelihood estimate of *b* in the formula logN=*a* − *b*M and its confidence limits [J]. Bulletin of the Earthquake Research Institute University of Tokyo, 1965, 43: 237−239.
[56] SCHULTZ R, ATKINSON G, EATON D W, et al. Hydraulic fracturing volume is associated with induced earthquake productivity in the Duvernay play [J]. Science, 2018, 359(6373): 304−308. DOI: 10.1126/science.aao0159.
[57] SHARMA P K, SINGH T N. A correlation between P-wave velocity, impact strength index, slake durability index and uniaxial compressive strength [J]. Bulletin of Engineering Geology and the Environment, 2008, 67(1): 17 − 22. DOI: 10.1007/s10064-007-0109-y.
[58] YAGIZ S. P-wave velocity test for assessment of geotechnical properties of some rock materials [J]. Bulletin of Materials Science, 2011, 34(4): 947 − 953. DOI: 10.1007/s12034-011-0220-3.
[59] ZHANG Jin-yuan, SHEN Yan-jun, YANG Geng-she, et al. Inconsistency of changes in uniaxial compressive strength and P-wave velocity of sandstone after temperature treatments [J]. Journal of Rock Mechanics and Geotechnical Engineering, 2021, 13(1): 143 − 153. DOI: 10.1016/j.jrmge.2020.05.008.
[60] ZHANG Fan, ZHANG Yu-hao, YU Yu-dong, et al. Influence of cooling rate on thermal degradation of physical and mechanical properties of granite [J]. International Journal of Rock Mechanics and Mining Sciences, 2020, 129: 104285. DOI: 10.1016/j.ijrmms.2020.104285.
[61] JIN Pei-hua, HU Yao-qing, SHAO Ji-xi, et al. Influence of different thermal cycling treatments on the physical, mechanical and transport properties of granite [J]. Geothermics, 2019, 78: 118 − 128. DOI: 10.1016/j.geothermics.2018.12.008.
[62] ZHU Zhen-nan, RANJITH P G, TIAN Hong, et al. Relationships between P-wave velocity and mechanical properties of granite after exposure to different cyclic heating and water cooling treatments [J]. Renewable Energy, 2021, 168: 375−392. DOI: 10.1016/j.renene.2020.12.048.
[63] SIRDESAI N N, SINGH T N, RANJITH P G, et al. Effect of varied durations of thermal treatment on the tensile strength of red sandstone [J]. Rock Mechanics and Rock Engineering, 2017, 50(1): 205−213. DOI: 10.1007/s00603-016-1047-4.
[64] GAUTAM P K, VERMA A K, SHARMA P, et al. Evolution of thermal damage threshold of jalore granite [J]. Rock Mechanics and Rock Engineering, 2018, 51(9): 2949 − 2956. DOI: 10.1007/s00603-018-1493-2.

(Edited by ZHENG Yu-tong)

中文导读

单轴压缩下热处理花岗岩的损伤特征：来自主/被动超声技术的见解

摘要：为了探明热处理对花岗岩损伤破裂的影响，对室温(25 ℃)及热处理(200，300和400 ℃)花岗岩试样进行单轴压缩试验，并采用主动超声和被动声发射监测技术研究试样的损伤特征。研究结果表明：与未进行热处理的试样相比，试样经200 ℃处理后单轴抗压强度(UCS)无明显变化，经300 ℃处理后UCS增加12.65%，经400 ℃处理后UCS降低4.97%。随着热处理温度由25 ℃升至400 ℃，试样初始P波速度由4909 m/s逐渐降低至3823 m/s，未加载时花岗岩试样的波速各向异性ε由0.03增至0.09。随着轴向荷载增加，ε受预存裂纹(包括热致裂纹)和应力诱发裂纹影响，在裂纹闭合阶段和不稳定开裂阶段迅速增大。超声波主频幅值在垂直方向(轴向)随应力增大而增大，在水平方向随应力增大而减小。此外，经热处理后试样的声发射事件定位震级减小，低频事件和高振幅事件增多。然而，没有足够的证据表明400 ℃以下的热处理对声发射时序特征、震源位置和*b*值有显著影响。

关键词：单轴压缩；热处理；声发射；超声波；*b*值；主频